Journal of Nuclear Materials 415 (2011) 189–197

Contents lists available at ScienceDirect

Journal of Nuclear Materials

journal homepage: www.elsevier.com/locate/jnucmat

Microstructural characterization and pore structure analysis of nuclear graphite

J. Kane [a,b,*], C. Karthik [a,b], D.P. Butt [a,b], W.E. Windes [b,c], R. Ubic [a,b]

[a] Department of Materials Science and Engineering, Boise State University, 1910 University Drive, Boise, ID 83725, United States
[b] Center for Advanced Energy Studies, 995 University blvd., Idaho Falls, ID 83415, United States
[c] Idaho National Laboratory, 2351 N. Boulevard, Idaho Falls, ID 83415, United States

ARTICLE INFO

Article history:
Received 18 March 2011
Accepted 28 May 2011
Available online 13 June 2011

ABSTRACT

Graphite will be used as a structural and moderator material in next-generation nuclear reactors. While the overall nature of the production of nuclear graphite is well understood, the historic nuclear grades of graphite are no longer available. This paper reports the virgin microstructural characteristics of filler particles and macro-scale porosity in virgin nuclear graphite grades of interest to the Next Generation Nuclear Plant program. Optical microscopy was used to characterize filler particle size and shape as well as the arrangement of shrinkage cracks. Computer aided image analysis was applied to optical images to quantitatively determine the variation of pore structure, area, eccentricity, and orientation within and between grades. The overall porosity ranged between ~14% and 21%. A few large pores constitute the majority of the overall porosity. The distribution of pore area in all grades was roughly logarithmic in nature. The average pore was best fit by an ellipse with aspect ratio of ~2. An estimated 0.6–0.9% of observed porosity was attributed to shrinkage cracks in the filler particles. Finally, a preferred orientation of the porosity was observed in all grades.

1. Introduction

Graphite is an important component to the design of high-temperature gas-cooled reactors. Many of these reactors use graphite as a neutron moderator and/or structural component such as fuel- and gas-coolant channels [1–3]. Graphite is a desirable material because of its low neutron absorption cross-section and its high-temperature strength [4]. During operation, material properties and dimensions can change as a function of neutron irradiation dose and temperature. Gradients in both temperature and dose can lead to significant stress and distortion of the graphite components. Over time these stresses and distortions, if unaccounted for, can lead to failure of components, blockage of coolant channels, and even restriction of control rod sleeves [5].

The nuclear graphite is typically a nearly isotropic polycrystalline material with its microstructure primarily composed of coke filler and binder [6]. Most of the nuclear grades contain a petroleum- or pitch-based coke. Materials such as graphite are quite unique in that variations in the coke type, quantity (relative to binder and later densification impregnations), forming process, and heat treatment processes can produce a relatively widespread distribution of initial properties and variation of graphite behavior under irradiation [2,7,8].

Irradiation-induced changes in graphite are strongly linked to the virgin microstructure of the graphite component [3,9]. The filler and binder phases, pore and crack microstructure, as well as their relative quantities will significantly impact the dimensional change, mechanical and thermal properties, and oxidation of the graphite upon irradiation. Given the variability in graphite initial properties, and consequently irradiation behavior, it is important to establish a thorough understanding of the fundamental mechanisms involved in irradiation-induced changes to properties and dimensions [9–13]. This task is best accomplished through thorough characterization of virgin and irradiated nuclear graphites. This work focuses on virgin nuclear graphite characterization via optical imagery and digital image analysis.

While digital image processing and digital image analysis have been around since the 1960s [14], they have just recently become more common in the nuclear industry. Image analysis has been used to determine microstructural inputs for fracture models of polygranular graphite [15] and more recently to characterize porosity development under varying oxidation conditions [16]. Additionally, digital image analysis has been applied to 3D X-ray tomography techniques to map density evolution in oxidized samples [17–19]. In this work image analysis is used to estimate 2D parameters of the macro-porosity including area, perimeter, shape, and orientation in virgin nuclear graphite grades. 2D image analysis while somewhat restricted in terms of directly accessible parameters, compared to a 3D analysis, is much quicker and capable of examining much larger samples. This allows for a detailed

* Corresponding author at: Department of Materials Science and Engineering, Boise State University, 1910 University Drive, Boise, ID 83725, United States.
E-mail address: joshuakane@u.boisestate.edu (J. Kane).

0022-3115/$ - see front matter © 2011 Elsevier B.V. All rights reserved.
doi:10.1016/j.jnucmat.2011.05.053

statistical description of the features of interest, which will greatly benefit later irradiated and oxidized graphite characterizations.

2. Experimental

Nuclear graphite grades IG-110, PGX, NBG-18, and PCEA were selected for characterization. NBG-18 and PCEA were chosen because of the Next Generation Nuclear Plant (NGNP) program's interest for high irradiation dosage regions of the Very High Temperature Reactor (VHTR) [2,3]. IG-110 is a fine grained historical reference grade which is currently being used in the HTTR and HTR-10 and is in many ways similar to IG-430, also a high dose candidate for the VHTR. PGX is a candidate grade for low dosage regions of the VHTR reactor. Pertinent data regarding these grades are presented in Table 1.

2.1. Sample preparation

Samples prepared for optical microscopy and pore analysis were approximately 0.2 cm thick and had an observable surface of approximately 2.25 cm^2. To strengthen the graphite samples internally and prevent degradation of graphite pore walls and surface flow during polishing, samples were impregnated with epoxy resin and allowed to cure for 24 h. The graphite samples were hand-polished with successively finer SiC abrasive paper to a final grit of 1200. Next, samples were placed without additional weight into a vibratory polisher and allowed to polish for 3 h in a 0.3 μm SiC water-based suspension. Upon completion, samples were cleaned with deionized water to remove remaining SiC abrasive.

2.2. Optical microscopy and image analysis

Optical microscopy was carried out using a standard bench-top Olympus BX51 Optical Microscope. Programming and code execution for pore identification and analysis were carried out using MATLAB® (MathWorks, USA) and its image processing toolbox. The bright field micrographs used for pore analysis were taken at a magnification of 5×. The pixel resolution of micrographs used for pore analysis was ~0.7 μm. The smallest pores identified were in the range of 5 μm^2; however, sample artifacts of similar sizes were also observed. To distinguish between porosity and sample artifacts of small sizes, higher magnifications were needed;

Table 1
Grain size refers to filler particle size.

Grade	Coke source	Forming process	Grain size	Vendor
PGX	Petroleum	Molded	Medium	Graftech, USA
PCEA	Petroleum	Extruded	Medium	Graftech, USA
NBG-18	Pitch	Vibration molded	Medium, 1.6 mm[a]	SGL, Germany
IG-110	Petroleum	Isostatic pressed	Superfine, 20 μm[b]	Toyo Tanso, Japan

[a] Maximum diameter of filler particles.
[b] Average particle length.

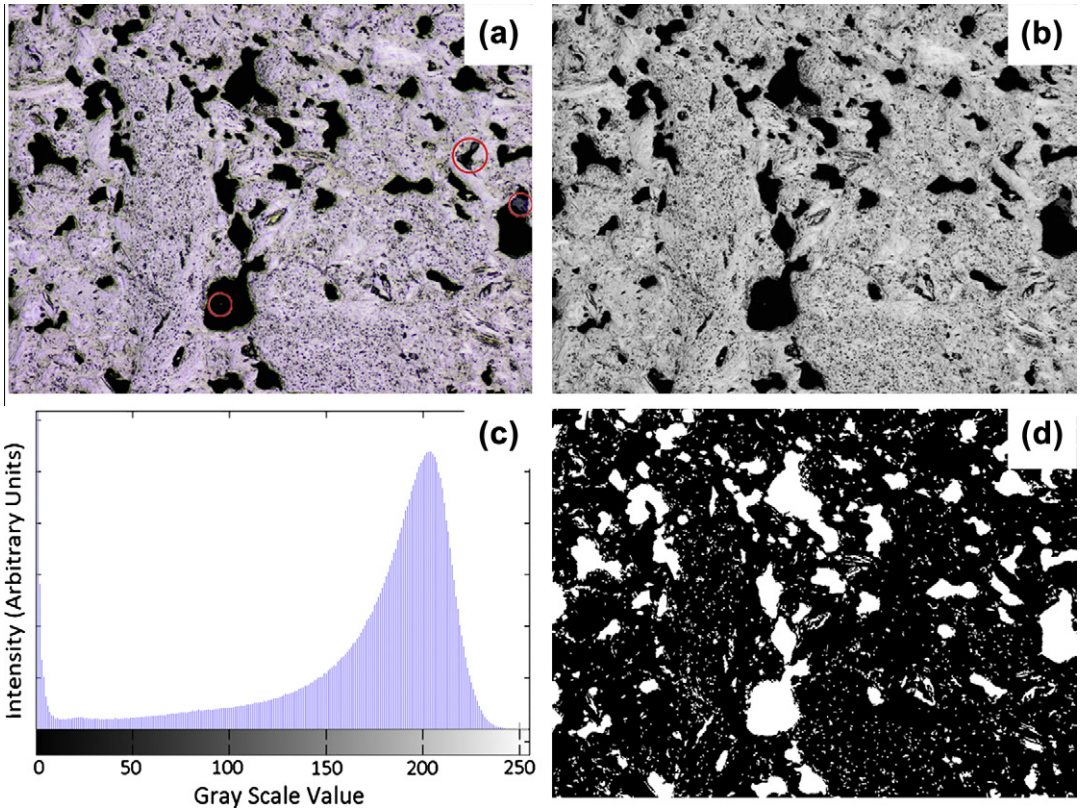

Fig. 1. Basic image processing flow: (a) original colored micrograph, (b) grayscale micrograph of (a) hue and saturation removed but luminance retained, (c) histogram of (b) prior to contrast stretching and thresholding, (d) final binary image, this image is ran through connective components algorithm to extract quantitative pore data.

therefore, the minimum pore size measured in this work was arbitrarily set to 12.5 μm^2. It was not necessary to use higher magnification in the case of such pores. Original micrographs were formatted as 24-bit color files as shown in Fig. 1a for PGX graphite. Upon uploading files to MATLAB they were converted to 8-bit grayscale images. The color to grayscale transformation was accomplished by eliminating the hue and saturation information while retaining the luminance of the color image (Fig. 1b). Fig. 1c shows a histogram of the grayscale image in Fig. 1b, in which two distinct peaks can be seen near 0 and 220 corresponding to the porosity and graphitic material respectively. Each graphite grade produced a nearly identical histogram. Contrast stretching was applied to all grayscale images. The reference points for contrast stretch were approximately 50 and 220 respectively. The lower reference of ~50 was chosen because it corresponded well with a local minima, yet it was still well within the range of what could sensibly be determined as porosity. The upper reference was chosen to correspond with the peak intensity of the polished graphitic material. Contrast stretching was performed to increase the sensitivity of the threshold parameter used for converting the images to the binary image matrices (Fig. 1d). Typical values for the threshold parameter (allowable values are normalized between 0 and 1 over the 8 bit range of 0–255) were 0.45 for PGX, NBG-18, and PCEA and 0.37 for IG-110.

Two additional processing steps were used between converting to a binary image and data collection. The first was removal of small pores of area less than 25 μm^2 using morphological opening. Next was the removal of small "islands" such as those circled in Fig. 1a. This step involved the use of a morphological flooding algorithm. These "islands" were removed under the assumption that they were (1) loose graphite fragments that become lodged in pores, or (2) artifacts of the 3D nature of the pores which were not directly in the polished plane of the sample.

To identify each pore and its respective pixels from the binary matrix, a connective components algorithm was applied with neighboring pixels defined as $N_4(p)$, the left, right, top, and bottom neighbor pixels [15]. Additional algorithms were used to extract the number of pixels (pixel area), the centroid coordinates within the matrix, perimeter, and orientation of each pore. Ellipses were used to provide a quantitative estimate of pore shape. The ellipse with the same normalized second central moment as the pore was used. The eccentricity (e), major axis length (M), minor axis length (m), and orientation of the major axis with respect to the horizontal image plane was extracted for each pore. The eccentricity of an ellipse is related to the major (M) and minor (m) axis length as,

$$e = \frac{\sqrt{M^2 - m^2}}{M}. \quad (1)$$

As such, eccentricity is defined between the degenerate cases of 0 and 1, where 0 is a circle and 1 is a line.

3. Results and discussion

3.1. Filler particle size analyses

The nature of the coke is integral to the development of the filler microstructure in nuclear graphite. As seen in Figs. 2–5, the shape of the filler particles varies from acicular to spherical. The shape of filler particles, in general, is a function of the coke's innate ability to align its rudimentary graphitic crystallites during calcination. Graphite with a petroleum-based coke tends to have anisotropic, acicular particles resulting from a high degree of alignment of rudimentary crystallites. On the other hand, pitch cokes are, in general, more isotropic and spherical in nature as a result of their lesser degree of rudimentary crystallite alignment. A summary of the size and shape of the filler material for each grade is given in Table 2.

The filler observed in IG-110, a fine grained, petroleum based, nuclear graphite appears acicular (Fig. 2). The mean length of filler observed was 27 ± 2 μm with a standard deviation (σ) of 22 μm.

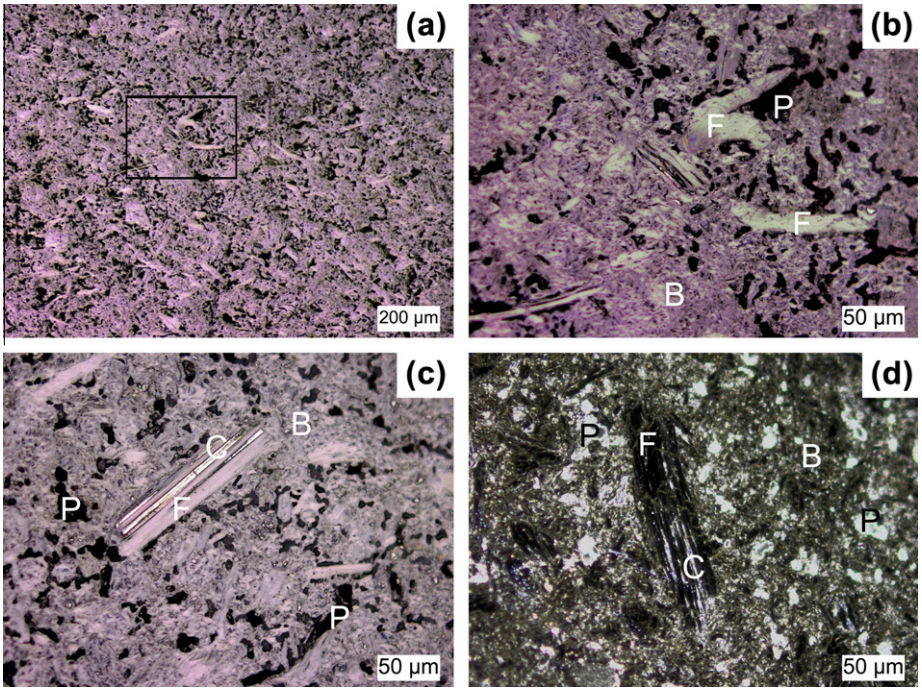

Fig. 2. Optical micrographs of IG-110 graphite: (a) typical bright field micrograph of IG-110 showing filler, binder, and porosity, (b) bright field micrograph showing magnified view of the highlighted region in (a), (c) bright field micrograph of filler where the bright regions running along length of filler particle are shallow shrinkage cracks and (d) dark field micrograph. P-Porosity, F-Filler, B-Binder, C-Shrinkage crack.

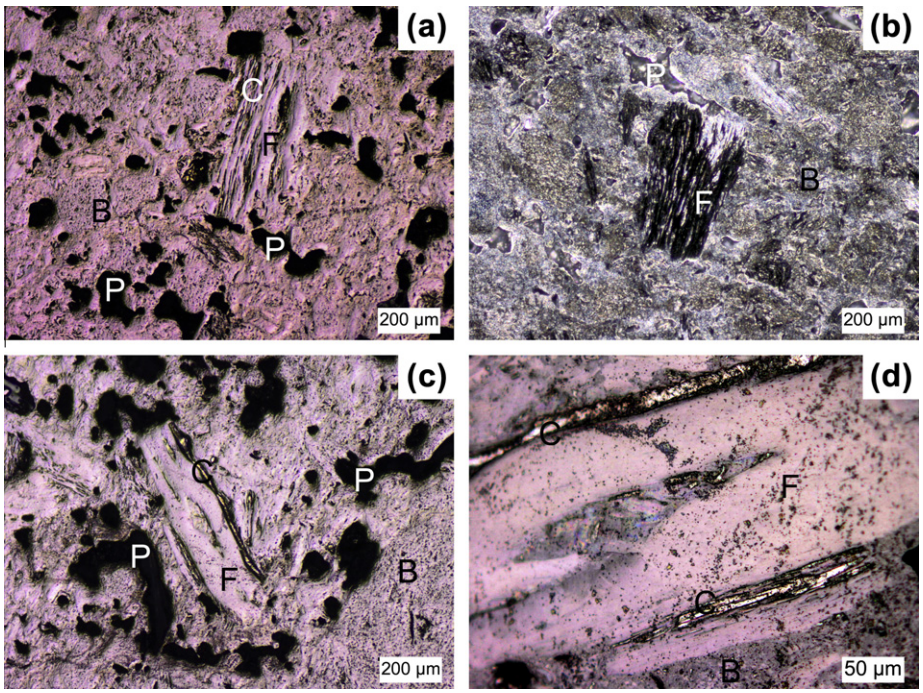

Fig. 3. Optical micrographs of PGX graphite: (a) typical bright field micrograph of PGX showing filler, binder, and porosity, (b) dark field micrograph of filler in binder matrix, (c) bright field micrograph of filler with long shrinkage cracks running parallel to particle long axis, and (d) bright field micrograph magnifying (c) P-Porosity, F-Filler, B-Binder, C-Shrinkage crack.

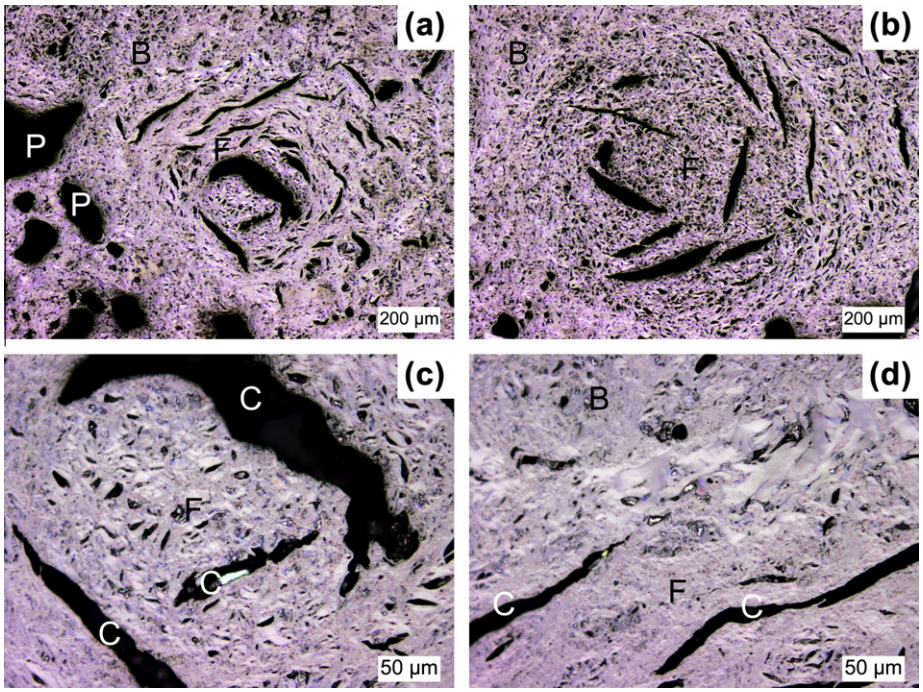

Fig. 4. Optical micrographs of NBG-18 graphite: (a) bright field micrograph showing filler particle, binder, and porosity, (b) bright field micrograph of filler surrounded by binder matrix, (c) bright field micrograph magnifying the inner region of filler particle in (a), and (d) bright field micrograph magnifying the outer perimeter of filler particle in (a). P-Porosity, F-Filler, B-Binder, C-Shrinkage crack.

This is reasonably similar to the average length given by the manufacturer of 20 μm. The mean aspect ratio observed for IG-110 filler is 3.9 ± 0.2, σ = 2.4. Observed in Fig. 2c are shrinkage cracks that run parallel to the major axis length of the particle. These cracks form during calcination as a result of the establishment of rudimentary basal planes of carbonaceous material. This strongly suggests that the *c*-direction of the graphitic crystallites is aligned with the minor axis of the particles.

The filler in PGX is also petroleum-based graphite. It is acicular much like IG-110 but, significantly larger in size (Fig. 3). PGX filler

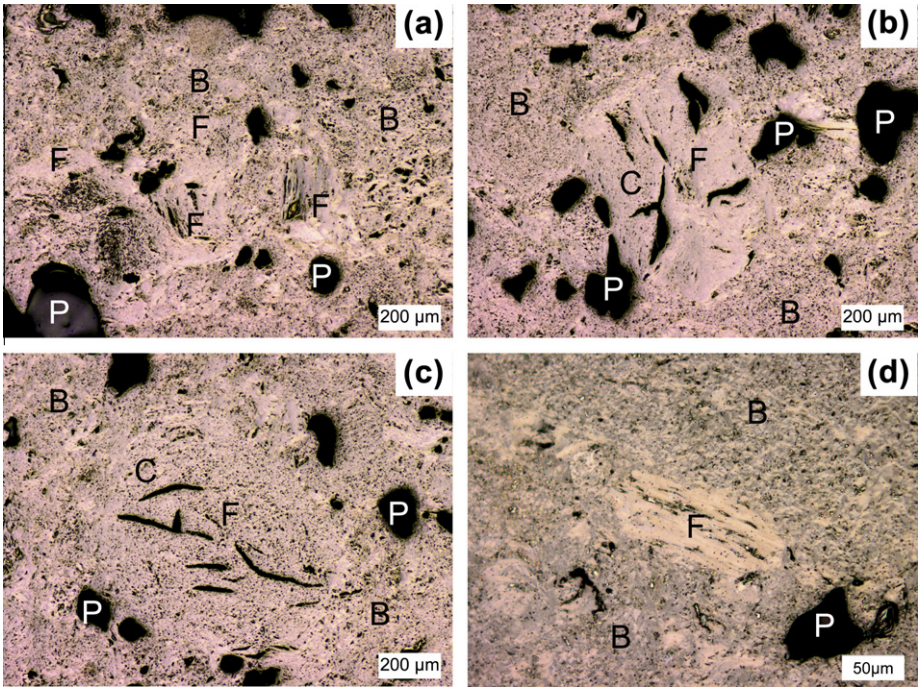

Fig. 5. Optical micrographs of PCEA graphite: (a) bright field image showing filler particles with various shapes, (b) bright field micrograph of filler with relatively high degree of crystallite alignment surrounded by binder matrix, (c) bright field micrograph of roughly spherical filler particle, and (d) bright field image of relatively small acicular filler particle. P-Porosity, F-Filler, B-Binder, C-Shrinkage crack.

Table 2
Measurements of observed filler material. Major axis length (MAL), standard deviation (σ), aspect ratio (AR).

Grade	Sample size	Mal mean[a] (μm)	Mal σ (μm)	AR mean[a]	AR σ
PGX	624	92 ± 7	85	3.1 ± 0.1	1.6
PCEA	320	126 ± 10	94	2.6 ± 0.2	1.6
NBG-18	300	360 ± 25	217	~1	–
IG-110	625	27 ± 2	22	3.9 ± 0.2	2.4

[a] Means are two sided confidence intervals, $\alpha = 0.05$.

particles are approximately three times larger than in IG-110 with a length of 92 ± 7 μm and σ = 85 μm. The aspect ratio of PGX filler was 3.1 ± 0.1 with σ = 1.6. Shrinkage cracks in PGX are more numerous and of greater thickness than those observed in IG-110.

The filler material in NBG-18, pitch-based graphite, appears to be spherical in nature (Fig. 4). The mean particle size observed in NBG-18 is 360 ± 25 μm with σ = 217 μm. The maximum particle size observed was 1796 μm which corresponds roughly with the manufacturer's stated maximum particle size of 1600 μm. The roughly 200 μm difference may in part be due to the difficultly in defining an exact particle boundary. The nearly spherical nature of the NBG-18 filler material suggests a relatively low degree of crystalline alignment within the particles. The crystallites in the center of the particles, in general, appear to be small and randomly oriented (Fig. 4b). Those toward the particle exterior appear larger with their long axis aligned with the particle circumference.

The shrinkage cracks in NBG-18 vary greatly in size. Many of the larger shrinkage cracks, as observed in Fig 4a and b, are oriented with their long axis approximately tangential to the particle's radial direction. Further magnification of the filler particles in Fig. 4a, c and d show the orientation of the small shrinkage cracks in the interior of the filler particle and near the perimeter respectively. The small shrinkage cracks toward the center of the filler particles appear to be randomly oriented, while those near the perimeter of the particle appear to be oriented similar to the larger shrinkage cracks.

PCEA, a petroleum-based graphite, had a wide variation in observed filler particles (Fig. 5). Approximately 70% of filler is acicular in shape. The acicular particles had a mean length of 137 ± 12 μm with σ = 88 μm. The mean aspect ratio of the acicular particles is 3.2 ± 0.2 with σ = 1.4. The acicular particles in PCEA are slightly larger than those in PGX, but have a nearly identical aspect ratio. The spherical filler particles in PCEA had a mean diameter of 99 ± 21 μm with σ = 102 μm. PCEA filler material appears to have varying degrees of crystalline alignment. The spherical filler particle shown in Fig. 5c appears to have crystalline alignment similar to that observed in the center of NBG-18 filler particles (Fig. 4). These crystallites are relatively small and have a random orientation. The crystallites observed in Fig. 5b appear to have a high degree of crystalline alignment similar to that observed in PGX particles (Fig. 3). The shrinkage cracks observed in PCEA were relatively narrow compared to cracks observed in NBG-18. The orientation appeared random for small shrinkage cracks. Large shrinkage cracks appeared to have a preferred orientation along the particles long axis for acicular particles (Fig. 5a and d). For spherical particles, the shrinkage cracks were aligned with one another, but not along any particular axis of the filler particle.

3.2. Pore structure analysis

The three different types of porosity within nuclear graphite are gas-evolved pores, shrinkage cracks, and micro-cracks [8,20]. Pore characterization via image analysis used in the present study was able to resolve only gas evolved pores and shrinkage cracks. As observed in Figs. 2–5, the porosity varies greatly in size, shape, and orientation between and within grades. A statistical summary of the data collected is given in Table 3.

Table 3 is the culmination of multiple samples of each grade covering areas of approximately 10 cm^2 for IG-110, NBG-18, and PCEA and an area of roughly 5 cm^2 for PGX. Such areas provided both large pore counts (on the order of 10^6) and were sufficient to observe variation within a grade. The arithmetic mean indicates

Table 3
Statistical summary of pore analysis. Mean is arithmetic mean. W. Mean is weighted mean based on each pore's fractional contribution to total porosity.

Grade	Area (μm^2)					Eccentricity		Additional	
	Mean	W. Mean	σ	Min	Max	Mean	σ	Porosity (%)	Count
PGX	197.9	21,400	2047	12.1	353,336	0.820	0.14	21.49	475,981
PCEA	146.8	30,100	2097	12.1	447,960	0.814	0.14	15.98	1,242,597
NBG-18	168.3	23,600	1986	12.1	505,123	0.816	0.14	13.97	916,076
IG-110	98	485	195	12.1	27,868	0.798	0.14	14.73	1,532,451

that the distribution in pore size is skewed greatly toward the minimum pore size compared to a normal distribution. Examination of the weighted mean suggests that the majority of the total porosity is a result of a minute quantity of large pores in PGX, PCEA, and NBG-18. In IG-110 the opposite appears to be true. The majority of the total porosity results from smaller pores as suggested by the weighted average. The mean eccentricity of the pores ranged from 0.798 for IG-110 to 0.82 for PGX, corresponding to aspect ratios of 1.66 and 1.75 respectively. A somewhat unexpected result was seen in the calculated porosities of the grades. NBG-18 was calculated to have an overall porosity of 14%, followed by IG-110 with 15%, PCEA with 16%, and PGX with 21% porosity. This result was unexpected given that visual inspection of IG-110 does not reveal significant porosity, while porosity is very apparent in NBG-18. The porosity was calculated by dividing the total pore area by the total area observed. For this calculation to be valid, the porosity must be nearly uniform throughout the graphite block. Using the theoretical densities of each graphite grade, apparent densities were back-calculated and compared to their respective values from the manufacturer (Table 4).

Table 4
Summary of experimental and manufacturer values for apparent density. Theoretical density calculated from lattice parameters.

Grade	Experimental (g/cm^3)	Manufacturer (g/cm^3)	Theoretical (g/cm^3)
PGX	1.772	–	–
PCEA	1.896	1.84	2.257
NBG-18	1.938	1.85	2.253
IG-110	1.925	1.77	2.257

Table 5
Tabulated standard deviations from fit of a normal distribution, with $\alpha = 0.05$, to the pore orientation distributions. Slight preferential orientation of long axis of pore observed. Sample population per face ranged from a minimum of ~87,000 pores to ~327,000 pores.

Grade	Face 1	Face 2	Face 3
PCEA	52.37 ± 0.14	49.19 ± 0.16	48.87 ± 0.17
NBG-18	49.82 ± 0.23	49.74 ± 0.17	47.82 ± 0.15
IG-110	51.75 ± 0.13	50.68 ± 0.13	43.00 ± 0.11

The experimental apparent densities were all in excess of those listed by the manufacturer. For IG-110, NBG-18, and PCEA the errors, relative to the manufacturer's value, were 8.8%, 4.8%, and 3.1% respectively. This positive error may occur as a result of an overestimation of pore area due to the choice of thresholding parameters. In a nuclear grade such as IG-110, size and proximity of the porosity can lead to connection of pores after thresholding. Such errors can be minimized, or at least remove experimentor bias to some degree, by investigation of automated global thresholding methods [15,21]. It is however, at least from visual inspection of optical micrographs, difficult to accept that manufacturer reported porosity of IG-110 is very similar to that predicted for PGX. Another possibility is the manufacturer's values were derived from fluid intrusion methods that were incapable of accessing all of the porous volume. This would result in an underestimation of the apparent densities. Regardless, this comparison is made to show the relative accuracy of measurements via digital image analysis.

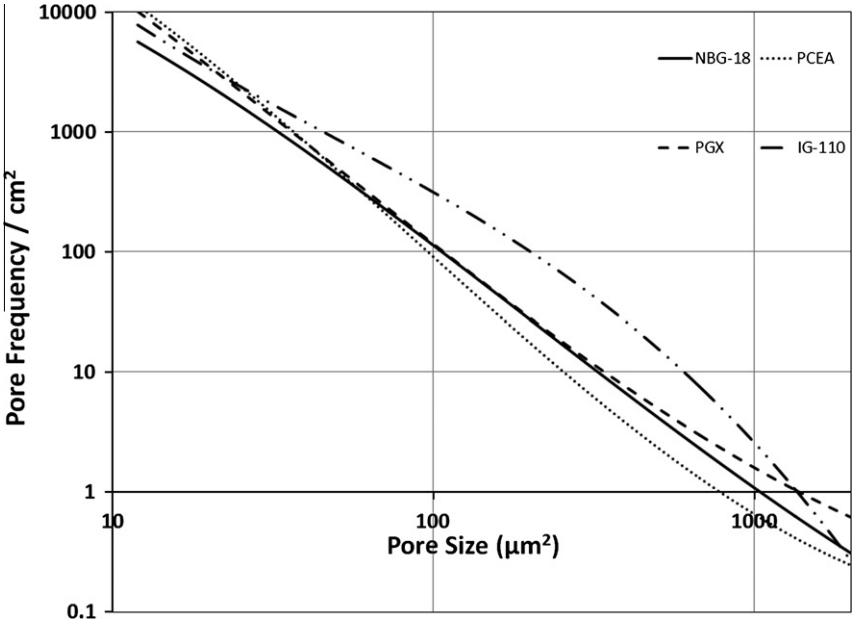

Fig. 6. Log–log plot of frequency of pore size per cm^2 as a function of pore size.

Inspection of the resulting data for pore orientation showed an approximately normal distribution of orientation with respect to the horizontal image plane. To confirm the existence of a preferred orientation within the porosity, three mutually orthogonal samples were taken from each grade (IG-110, NBG-18, and PCEA). Resulting orientations were fitted to normal distributions and the standard deviation, σ, for each sample was tabulated. As seen in Table 5, NBG-18 and PCEA have only two statistically different standard deviations, implying a preferential orientation of porosity within the grades. IG-110 has three statistically significant means; however, two are relatively close to one another. This is assumed to be a result of imperfect slicing along the three orthogonal planes resulting in slight displacements of the standard deviations from their true values. While this (Table 5) indicates the existence of preferential pore orientation, it does not provide significant evidence as to the magnitude or variation of the orientation upon processing of the original block. To obtain such, detailed information about sampling location relative to the original block and the blocks orientation relative to processing would need to be known. It should be noted that there was no significant change in the distribution of pore area or shape with sample position or orientation. The orientation distribution observed in each cross-section does not appear to change as a function of pore area.

Since proprietary details of processing are only approximately known for each grade, it is difficult to conclude the exact reasoning for the observed pore orientation; however, it is suspected that the orientation is the result of densification impregnations. Gas evolved from the impregnation material will take the path of least resistance corresponding to the path through the impregnated pores to the nearest surface. If all three orthogonal faces are equally far from the point of gas evolution, there will be no preferred alignment of the porosity. When the point of gas evolution has different path lengths to the graphite block surface, preferred alignment will result. Using this hypothesis, the degree of preferred orientation will be dependent upon the position of the examined sample with respect to the original graphite block.

While useful, the statistical data above does not fully describe the nature of the pores within each grade. The quantity of pores within any given size range was found to be a strong function of pore size. The shape of porosity, while not strongly dependent on pore size, had a wide distribution. In general, the aspect ratio of a pore ranged from 1 to 25. To better describe pore quantities and shape, continuous distributions were fitted to the experimental data collected. A plot of pore frequency/cm^2 vs. pore area ranging from 12 μm^2 to 2000 μm^2 is shown in Fig. 6. Although significantly larger pores were observed in each grade, more than 98% of the pore data fell within this range. The ~2% remaining was discarded to allow a 'better' fit of the remaining data. Initial inspection of plotted data displays the approximate "power-like" nature of pore frequency vs. size. Transformation of the dependent and independent variables by a natural logarithm yield approximately linear functions (Fig. 6). The pore area, while expressed in units of μm^2, was really measured as a discrete function of pixel quantities.

The final distributions were deemed best fit by a third-order polynomial with the natural log of the pore area as the independent variable (Table 6).

Table 6
Coefficients for fitting area distributions of each graphite grade. X is pore area in μm^2. Y is frequency per cm^2 from Eq. (2).

Grade	a	b	c	d
PGX	13.416385	−1.220592	−0.240437	0.0211058
PCEA	12.045997	0.0249847	−0.552325	0.0416005
NBG-18	11.072113	−0.26909	−0.339038	0.0213758
IG-110	15.431958	−3.794709	0.6107167	−0.05282

Table 7
Parameters for Johnson S_B fit of pore eccentricity.

Grade	γ	δ	θ	σ
PGX	−1.930488	1.0427341	−0.059312	1.0607131
PCEA	−1.948658	1.0762906	−0.080897	1.0810973
NBG-18	−1.883605	1.0386604	−0.050993	1.051878
IG-110	−1.862962	1.1055111	−0.068859	1.0690328

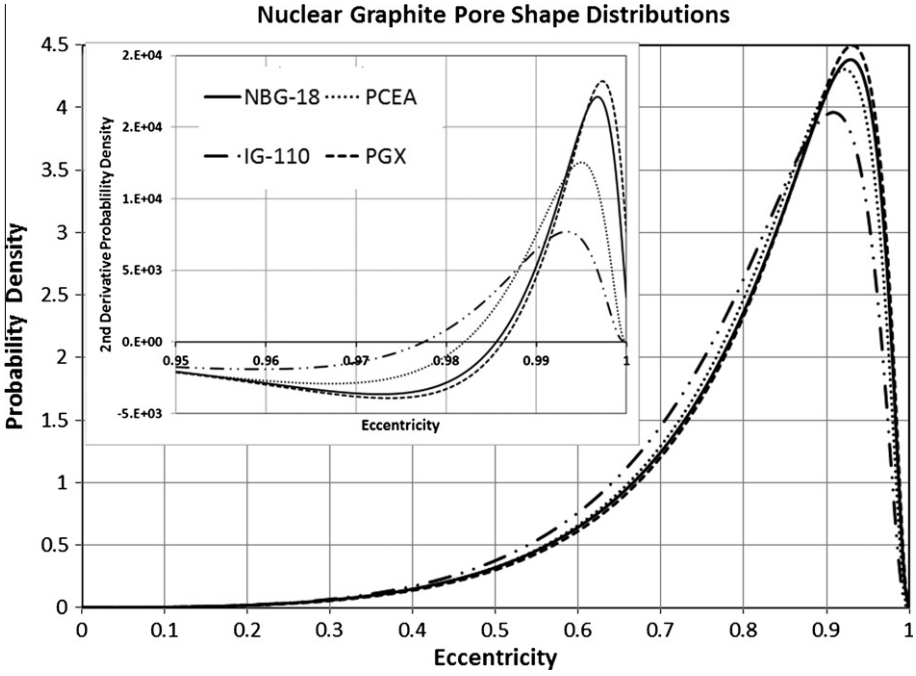

Fig. 7. Continuous probability distribution functions of porosity shape described by eccentricity of an ellipse. Inset plot is the 2nd derivative of the density function over the range of e = 0.95–1.

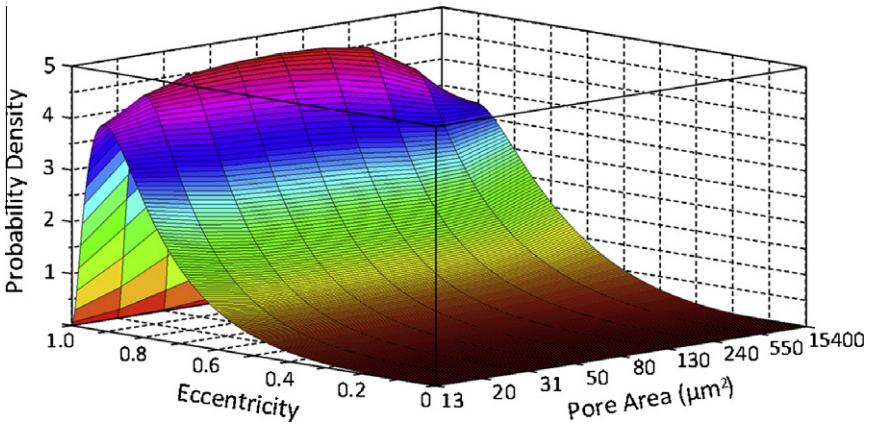

Fig. 8. 3D plot of the probability density of various pore shapes (eccentricity) for various ranges of pore area; the pore area given is the log-mean average of the range of pore areas used.

$$ln(y(x)) = a + bln(x) + cln(x)^2 + dln(x)^3 \quad (2)$$

Higher order polynomials provided higher R^2 values and lower root mean square errors; however, the rate of increase in 'fit improvement' dropped significantly with increasingly higher orders. The general logarithmic nature of the pore area distribution in PCEA appears to coincide well with similar image analysis techniques used by Contescu for PCEA [16].

The shape of the porosity as described by the eccentricity of an ellipse is shown in Fig. 7. By inspection, it is apparent that each grade has a relatively similar distribution, with the largest deviation occurring in the curve for IG-110. This deviation of IG-110 from the other grades is hypothesized to be the result of the green body formation via isostatic press. Fig. 7 suggests that only a minority of the total pores may be described as approximately spherical (~6%) while nearly 75% of the pores examined have aspect ratios between 1.5 and 5. The average aspect ratio of porosity in nuclear graphite is approximately 1.7 and ranges from a low of 1.66 for IG-110 to a high of 1.75 for PGX.

The shape of the experimental data curve for eccentricity was best fit by the Johnson S_B continuous distribution function. The Johnson S_B follows the general form,

$$f(x) = \frac{\delta}{b(1-b)}\phi(z) \quad (3)$$

where $z = \gamma + \delta \ln(b/1-b)$, with $b = (x-\theta)/\sigma$, and ϕ is the standard normal distribution (Parameters in Table 7). For this function, γ and δ are shape parameters while θ and σ define the location and shape of the curve, respectively. The peaks of each function are located at eccentricities of 0.908, 0.931, 0.929, and 0.922 (aspect ratios of 2.389, 2.747, 2.704, and 2.579) corresponding to IG-110, PGX, NBG-18, and PCEA respectively. The probability of a pore existing with an eccentricity less than that of peak density is approximately 0.78 and ranges from 0.773 to 0.797.

Since two types of pores were observed, gas-evolved porosity and shrinkage cracks, with very different shapes, it was initially hypothesized that the pore shape distribution would be bimodal. As seen in Fig. 7, this hypothesis is invalid. The shape distribution of porosity in nuclear grade graphite shows no obvious transition between shrinkage cracks and gas evolved porosity. To estimate the shrinkage crack contribution to total porosity the following assumption was made: The 2nd inflection point in the continuous distributions is located at the eccentricity value where shrinkage cracks become the dominant observation. Using this criterion it was found that shrinkage cracks account for a fraction greater than or equal to ~0.9% of IG-110 pores, ~0.6% of PGX pores, ~0.6% of NBG-18 pores, and ~0.8% of PCEA pores. This appears to visually coincide with the optical micrographs of each grade. The average aspect ratio of the inflection point was approximately 5.5.

From the examination of pore shape as a function of pore area, it was observed that the shape distribution function is slightly dependent on pore area. As the pore size increases, the probability density near the peak position increases and becomes a maximum near ~100 μm^2 for NBG-18 and PCEA (Fig. 8). For IG-110 this peak occurs at approximately 300 μm^2. There is also a slight shift in the peak position to higher eccentricities that occurs in each grade. As the pore area is increased, this shift becomes much smaller. While there is a slight dependence of the shape distribution on pore area, the overall fit is exceptional over the entire range of pore area.

4. Conclusions

This paper characterizes the virgin microstructure of filler material and porosity in nuclear grade IG-110, PGX, NBG-18, and PCEA. As expected, the IG-110 and PGX grades had anisotropic filler particles of super fine and medium size, respectively. The newer, nearly isotropic grades NBG-18 and PCEA had filler particles more spherical in nature. The filler particles of these grades vary from super fine anisotropic particles in IG-110 to medium isotropic filler particles in NBG-18. The degree of crystalline alignment, which ultimately determines the particle shape, can be compared for each grade by inspection of the aspect ratio of the particles.

Image analysis of porosity in nuclear graphite appears to be an accurate method for quantitatively determining distributions and trends within the porosity. Apparent densities were measured accurately by image analysis. Preferential alignment was observed in each grade as a result of the examination of three orthogonal samples of each grade. The area of macro-scale porosity is roughly logarithmic in nature and can be fitted well with a third-order polynomial. The distribution of eccentricity in macro-scale porosity is fitted with the Johnson S_B distribution.

While the size and shape of these 3D features may not be directly derived from measurements in 2D cross-sections, the measurements do provide a good qualitative basis for comparison with irradiated and oxidized graphite specimens.

Acknowledgments

This material is based upon work supported by the Department of Energy [National Nuclear Security Administration] under Award Nos. 00041394/00026 and DE-NE0000140. Furthermore, J. Kane acknowledges the funding of the Nuclear Regulatory Commission under the Nuclear Materials Fellowship Program (NRC-38-08-955).

References

[1] B.J. Marsden, Li H. Fok, Irradiation behavior and structural analysis of HTR/VHTR graphite core components, in: 18th International Conference on Structural Mechanics in Reactor Technology (SMiRT 18), China, Beijing, August 7–12, 2005. SMiRT18-A01-7.
[2] R. Bratton, W. Windes, NGNP graphite selection and acquisition strategy, ORNL/TM-2007/153-10-07 (INL/MIS-10-19427), Oak Ridge National Laboratory, July 28, 2010.
[3] W. Windes, T. Burchell, R. Bratton, Graphite technology development plan, INL/EXT-07-13165, Idaho National Laboratory, September 2007.
[4] B.T. Kelly, Physics of Graphite, Academic Press, New York and London, 1962.
[5] B.T. Kelly, B.J. Marsden, K. Hall, Irradiation Damage in Graphite due to Fast Neutrons in Fission and Fusion Systems, TECDOC-1154, International Atomic Energy Agency, Vienna, Austria, 2000.
[6] ASTM Standard D7219, 2008, Standard specification for isotropic and near-isotropic nuclear graphites, ASTM International, West Conshohocken, PA, 2003, doi:10.1520/D7219-08.
[7] W.P. Eatherly, E.L. Piper, Manufacturing, in: R.E. Nightingale (Ed.), Nuclear Graphite, Academic Press, 1962, pp. 21–51.
[8] R.E. Nightingale, Structure, in: R.E. Nightingale (Ed.), Nuclear Graphite, Academic Press, 1962, pp. 87–115.
[9] R. Blackstone, J. Nucl. Mater. 65 (1977) 72–78.
[10] B.T. Kelly, A.J.E. Foreman, Carbon 12 (1974) 151–159.
[11] B.T. Kelly, Carbon 30 (1992) 379–383.
[12] B.T. Kelly, Carbon 32 (1994) 119–125.
[13] R.H. Telling, M.I. Heggie, Philos. Mag. 87 (2007) 4797–4846.
[14] R.C. Gonzalez, R.E. Woods, Digital Image Processing, third ed., Pearson Education Inc., New Jersey, 2008.
[15] T.D. Burchell, Carbon 34 (1996) 297–316.
[16] C.I. Contescu, T.D. Burchell, Characterization of porosity development in oxidized graphite using automated image analysis techniques, ORNL/TM-2009/192, 2009.
[17] L. Babout, P.M. Mummery, T.J. Marrow, A. Tzelepi, P.J. Withers, Carbon 43 (2005) 765–774.
[18] L. Babout, T.J. Marrow, P.M. Mummery, P.J. Withers, Scr. Mater. 54 (2006) 829.
[19] A. Hodgkins, Mater. Sci. Technol. 22 (2006) 1045.
[20] K. Wen, J. Marrow, B. Marsden, J. Nucl. Mater. 381 (2008) 199–203.
[21] N. Otsu, IEEE Syst. Man Cybern. 9 (1979) 62–66.